




Improvement on biocompatibility and corrosion resistance of a Ti₃Zr₂Sn₃Mo₂₅Nb alloy through surface nanocrystallization and micro-arc oxidation

Sen Yu^{1,2,*} , Depeng Zeng^{2,3}, Hui Zhu¹, Wei Zhang², Lan Wang³, Zhentao Yu², Wangtu Huo², Dagang Guo^{1,*}, Meili Zhang⁴, and Gui Wang⁴

¹ State Key Laboratory for Mechanical Behavior of Materials, School of Material Science and Engineering, Xi'an Jiaotong University, Xi'an 710049, People's Republic of China

² Shaanxi Key Laboratory of Biomedical Metallic Materials, Northwest Institute for Non-Ferrous Metal Research, Xi'an 710016, People's Republic of China

³ School of Materials Science and Engineering, Northeastern University, Shenyang 110004, People's Republic of China

⁴ Centre of Advanced Materials Processing and Manufacturing (AMPAM), The University of Queensland, St Lucia, QLD 4072, Australia

Received: 30 November 2021

Accepted: 28 January 2022

Published online:

8 February 2022

© The Author(s), under exclusive licence to Springer Science+Business Media, LLC, part of Springer Nature 2022

ABSTRACT

This paper reported a surface modification method to improve corrosion resistance and biocompatibility of a Ti₃Zr₂Sn₃Mo₂₅Nb alloy (named as TLM). A 100-μm-thick layer with an average grain size of 70 nm was created on the alloy surface through sliding friction treatment (SFT), followed by a micro-arc oxidation treatment (MAO) to create a porous coating. Phase composition, morphology, structural characteristics, and elemental characteristics of the MAO coating were inspected by scanning electron microscope (SEM), energy-dispersive spectrometer (EDS) and X-ray photoelectron spectroscopy (XPS). Corrosion resistance of the MAO coating was tested by electrochemical method, and the biocompatibility of the MAO coating was evaluated by cell adhesion and proliferation, and protein adsorption tests. It has found that the surface morphology and chemical composition of the MAO coating produced on the SFT surface (NG-MAO) were not significantly different from those of the MAO coating formed on the original TLM substrate without SFT (CG-MAO). However, the corrosion current density of the NG-MAO coating in 0.9% NaCl solution (PS) and simulated body fluid (SBF) solution decreased 43.4 and 46.7%, respectively, as compared to the CG-MAO coating. The polarization resistance

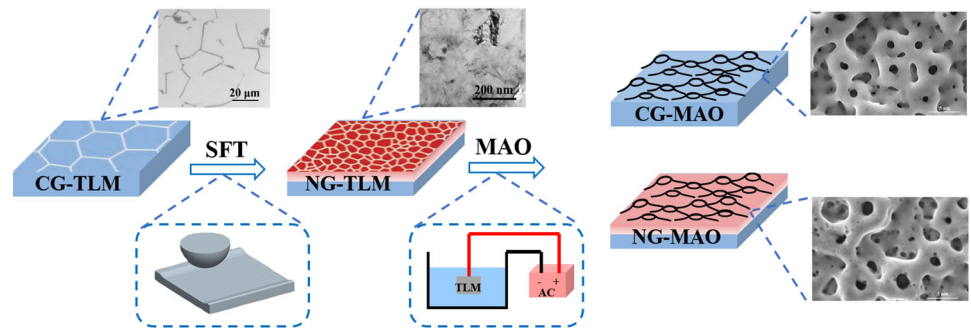
Handling Editor: Catalin Croitoru.

Prime Novelty Statement: This paper reported that a micro-arc oxidation coating was created on a nanograined layer induced by sliding friction treatment on a β-titanium Ti₃Zr₂Sn₃Mo₂₅Nb alloy. The nanocrystalline layer reduced the porosity and increased the thickness of the MAO coating, leading to an enhanced corrosion resistance. The specific porous structure and roughness are favorable for cells to adhere and grow in and enhanced the hydrophilicity to absorb proteins.

Address correspondence to E-mail: ninbrc@stu.xjtu.edu.cn; guodagang@mail.xjtu.edu.cn

of the NG-MAO coating was also 122% higher than that of the CG-MAO coating in PS. And the protein adsorption capacity and cell proliferation have been significantly increased on the NG-MAO coating compared to its counterpart, the CG-MAO coating.

GRAPHICAL ABSTRACT



Introduction

Beta-titanium (β -Ti) alloys composed of non-toxic elements have been explicitly developed over decades as implantable materials for the rational combination of the requisite characteristics in biomedical application [1, 2]. These characteristics include: (1) only biocompatible elements to avoid neurological disorders and toxicity in human tissues and promote bone integration after implantation [3, 4] and (2) appropriate microstructural features to meet the stringent requirements on load-bearing capability, fatigue performance and biomechanical compatibility with hard tissue [5, 6]. However, there are still concerns regarding the corrosion resistance of β -Ti alloys in the very harsh environment inside the human body which contains organic acids, alkaline earth metal ions (Na^+ , K^+ , Ca^{2+}), Cl^- ions, etc., coupled with protein, enzyme and cells [1, 6, 7]. Besides, due to the lack of biological activity, β -Ti alloys could not induce bone tissue growth and form qualified osseointegration to meet the requirements of long-term clinical services [1, 7, 8]. With the continuous increase in clinicians' and patients' expectation of shortening tissue healing time and improving long-term rehabilitation treatment outcomes, the

requirement to continuously improve and advance biomaterial has been raised [1, 8, 10].

It is proven that the surface bioactivity of the implant plays a dominant role to determine the osseointegration and the long-term bone integration of the implant [11–13]. Therefore, bioactive surface coating has been investigated as an effective way to solve the problem associated with the biological inertia of Ti alloy and improve bone integration efficiency and quality, with enormous efforts concluding that bone-like apatite layer induced by bioactive coating could form firm chemical bond with living bones [14–16]. At present, a variety of surface modification technologies have been developed to improve the surface bioactivity of hard tissue implants, including but not limited to sandblasting, thermal spraying, alkali treatment, surface mechanical attachment treatment (SMAT), self-assembly, laser surface modification and micro-arc oxidation (MAO) [17–20]. Furthermore, a combination of surface modification technologies could obtain coatings with further improved performance or multiple functions, which has become an important research direction of surface modification of Ti alloy implants [21–24].

Recently, composite MAO, which includes a surface nanopretreatment and then MAO on the pretreated surface, has been developed to improve

coating corrosion resistance and biocompatibility by changing matrix microstructure. Gu et al. [25] used ultrasonic forging to refine the surface grain of Ti6Al4V to 200 nm. The MAO coating obtained on such pretreated surface demonstrated smaller pore size, increased micro-hardness and improved corrosion resistance. And other research results also showed that surface nanocrystallization through pretreatment could improve MAO coating [26]. Sliding friction treatment (SFT) is a method of forming a nanocrystalline layer on a metal surface by controlling high hardness friction head to carry out reciprocating friction treatment on the material surface [27, 28]. SFT is capable of making grain structure change gradually from the top nanostructural surface to no-structure changed matrix without an obvious interface [29]. It has been intensively used to refine surface grain structure and improve mechanical behavior by surface severe plastic deformation. SFT has also been reported as a pathway to improve performance and service life of a range of biometallic materials [28, 29]. Zhang et al. [29] reported an SFT treatment result on a pure tantalum, including a gradient distribution of deformation layer along the depth, and fully equiaxed nanocrystals on the treated surface with an average grain size of 8 nm. Liu et al. [30] made nanocrystals with an average grain size of 98 nm on the surface of a Mg–Zn–Y–Ce–Zr alloy by SFT.

The Ti3Zr2Sn3Mo25Nb alloy (TLM) is a near β titanium alloy designed for a broad range of orthopedic application. It has low elastic modulus between 53 and 81 GPa and high tensile strength up to 1000 MPa with acceptable biocompatibility and biomechanical adaptability [31]. Like β -Ti alloys stated above, TLM also shares the shortcomings of inadequate bioactivity and corrosion resistance. So far, there have been few reports on the surface modification of TLM with composite coating method to address these issues. The current study aims to further improve its biocompatibility and corrosion resistance through a combination of SFT-induced surface nanocrystallization and MAO treatments. The SFT was first used to achieve nanocrystalline structures on the TLM surface, and then, MAO was carried out on the SFT-treated surface in an electrolyte containing bioactive elements of calcium and phosphorus. The effects of the nanocrystalline surface on the phase composition, microstructure, morphology,

corrosion resistance and bioactivity of the MAO coating were investigated.

Materials and method

Materials and surface treatment

TLM alloy sheets with a thickness of 5 mm were solution- and age-treated. The solution treatment was performed at 750 °C for 1 h followed by quenching into cold water. Ageing was carried out at 510 °C for 6 h and then air cooling to the room temperature. The temperature control during solution and ageing treatments was ± 1 °C. The chemical composition of the TLM alloy sheet is shown in Table 1. The phase composition was detected using optical microscope (Axiovert A1, Zeiss) and X-ray diffraction (XRD, D8 ADVANCE).

SFT was performed on the as-treated TLM sheets with a load of 350 N, 0.2 m/s in sliding velocity, 50 mm in amplitude, and 50 times for surface nanocrystallization. More details of the SFT process were reported elsewhere [26]. To eliminate the surface pollution from SFT, the top surface layer of 1–3 μm was removed by mechanical polishing carefully. The SFT-treated samples were grouped as the nanograined (NG) TLM. For comparison, the heat-treated samples without the SFT were grouped as the coarse-grained (CG) TLM.

Both the NG and CG sheets were cut into 10 mm \times 10 mm in size. MAO treatment was conducted to these samples in a stainless-steel tank where TLM sheet sample was fully immersed into an electrolyte composed of calcium acetate (18 g/L), sodium β -glycerophosphate (5 g/L) and deionized water. During the MAO treatment, the TLM sheet sample was worked as an anode, while the stainless-steel tank was a cathode. All the specimens were treated for 6 min at 390 V, 20% duty cycle, and 120 Hz frequency. The NG and CG TLM after MAO treatment were denoted as NG-MAO and CG-MAO, respectively.

Table 1 Chemical composition of the TLM alloy

Element	Nb	Zr	Mo	Sn	C	N	O	Ti
wt. %	25.2	3.01	2.94	2.0	0.01	0.02	0.14	Bal

Microstructure characterization

Microstructure of the NG and CG TLM was inspected by an optical microscope (Axio Vert A1, Zeiss), and a transmission electron microscope (TEM, JEM-2100) was used to characterize microstructure and phase composition of NG samples. The grain size was detected by the intercept method [27]. The surface morphology and cross section of MAO coating were observed by a scanning electron microscope (SEM, JSM-6460). An area of $30\ \mu\text{m} \times 30\ \mu\text{m}$ was randomly selected for imaging analysis using Image Pro Plus (IPP, media cybematics, 6.0). Five samples were randomly selected from each group for statistical analysis of porosity and pore distribution. Surface roughness and morphology of the MAO coatings were measured by an atomic force microscope (AFM, Dimension Icon) with the scanning range of $30\ \mu\text{m} \times 30\ \mu\text{m}$. Chemical characteristics of the surface and cross section of the two groups of samples were analyzed by energy-dispersive spectrometer (EDS, INGAX-sight), along with quantitative analysis of the elements using Inca software. The phase composition of MAO coating was determined by X-ray diffraction (XRD, D8 ADVANCE), and the phase structure was analyzed by Jade 6.5 software. X-ray photoelectron spectroscopy (XPS, Thermo ESCALAB 250xi) was used to analyze the surface element characteristics of the coatings. The hydrophilicity of CG-MAO and NG-MAO coatings was measured using a contact angle measuring instrument (JY-82, Dingsheng, China). Ultrapure water was used as the testing fluid, and at least three samples from each group were tested.

Electrochemical corrosion test

Open-circuit potential (OCP), electrochemical impedance spectroscopy (EIS) and potentiodynamic polarization curve (PDP) of CG-MAO and NG-MAO samples were tested using an electrochemical workstation (IM6, Zahner) in physiological saline (PS, 0.9 wt% NaCl aqueous solution) and simulated body fluid (SBF) solution, respectively.

Protein adsorption

Eight specimens from each group were put into a 24-well cell culture plate and washed in the wells for 3 times with phosphate-buffered saline (PBS) at $37\ ^\circ\text{C}$.

The specimens were incubated with 1 ml PBS containing 2.5% fetal bovine serum (Minhai Bio, Lanzhou, China) in each well at $37\ ^\circ\text{C}$, and four specimens were taken out after 7- and 14-day incubation, respectively. The adsorbed protein content (A_s) on the surface was measured by the Pierce™ BCA protein detection kit (Thermo-Scientific) and is calculated as follows:

$$A_s = A_0 - A_1 \quad (1)$$

where A_s is the protein adsorbed on the surface, A_1 is the protein left in the solution after adsorption, and A_0 is the protein in the culture medium without samples under the same culture conditions.

In vitro cell co-culture

The osteoblast cell line (MC3T3-E1) was selected for in vitro co-culture; the adhesion and proliferation of osteoblasts on the surface of the NG-MAO coating and the CG-MAO coating were detected by Live-Dead staining kit (L7012 LIVE/DEAD BacLight Bacterial Viability Kit) and AlamarBlue assay kit (Life Technologies). Two groups of samples were sterilized with 75% ethanol for 2 h, irradiated with UV for 30 min, and then placed in a 24-well culture plate. Tissue culture plate (TCP) was served as control. The cells were seeded on the surface with a density of 4000 cells/cm². After culturing for 1 and 3 days, AlamarBlue indicator was added into each well and incubated for 4 h. One hundred microliters of medium from each well was transferred to a 96-well black plate and passed the microplate reader (Spectramax i3, Molecular Devices) to record their fluorescence intensity. At least three samples were performed for each group. Live and dead cells were routinely stained by Live-Dead kit and observed by an upright fluorescence microscope (BX53, Olympus).

To observe cell morphology on the sample surface, after culturing for 1 and 3 days, the samples were washed with PBS for three times and fixed in 1 mL of 2.5% glutaraldehyde at $4\ ^\circ\text{C}$ for 30 min. The samples were washed for three times with PBS. Finally, the samples were dehydrated with graded ethanol aqueous solution containing 30, 50, 70, 80, 90, 95 and 100% ethanol, each for 15 min, and then freeze-dried. The morphology of the cells on the surface was observed with a scanning electron microscope (SEM, Quanta 250).

Statistical analysis

Each experiment was repeated at least five times, and the results were expressed as means \pm standard deviation. The statistical difference between two groups was analyzed by *t*-test, in which $p < 0.05$ represented a statistical difference, $p < 0.01$ represented a significant difference.

Results

Microstructure of the SFT surface

Optical metallography and XRD pattern of TLM after solution and aging treatment as shown in Fig. 1 revealed that the microstructure of the sheets was composed of β matrix and a small amount of acicular α , and the average grain size of the β matrix was around 40 μm . Optical metallographic image of the NG sample in Fig. 1b presented a 100- μm -thick

severely deformed layer where grains were highly elongated and refined. The TEM image of the top layer in Fig. 1c showed the randomly distributed elongated grains with an average grain size of 70 nm. The corresponding selected area electron diffraction (SAED) pattern as shown in Fig. 1d revealed that these fine nanocrystals were β -Ti. The XRD patterns of CG and NG in Fig. 1e showed that CG consisted of two phases of precipitated α phase and original β phase, while the NG sample only owned a single β phase, consistent with the TEM result.

Morphology and composition of the MAO coatings

Figure 2 shows the surface morphology of the MAO coatings on the NG and CG surfaces. As shown in Fig. 2a and b, the two surfaces were evenly distributed with sub-circular or elliptical crater-like pores in micron scale, and the chemical composition

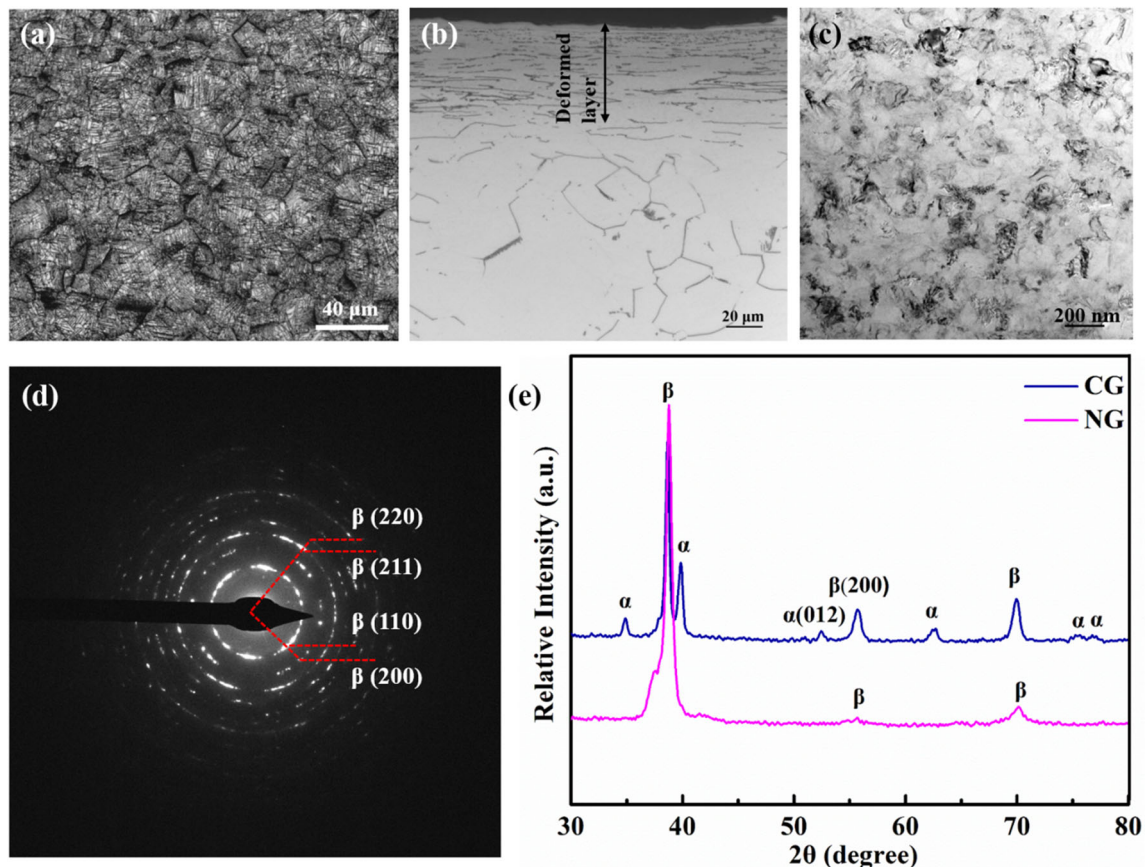


Figure 1 Microstructure and phase structure: **a** Optical metallographic image of the TLM alloy after solution and aging treatment, **b** optical metallographic image of cross section of NG

sample, **c** TEM bright-field image of NG sample, **d** SAED pattern of NG sample, and **e** XRD patterns of CG and NG TLM.

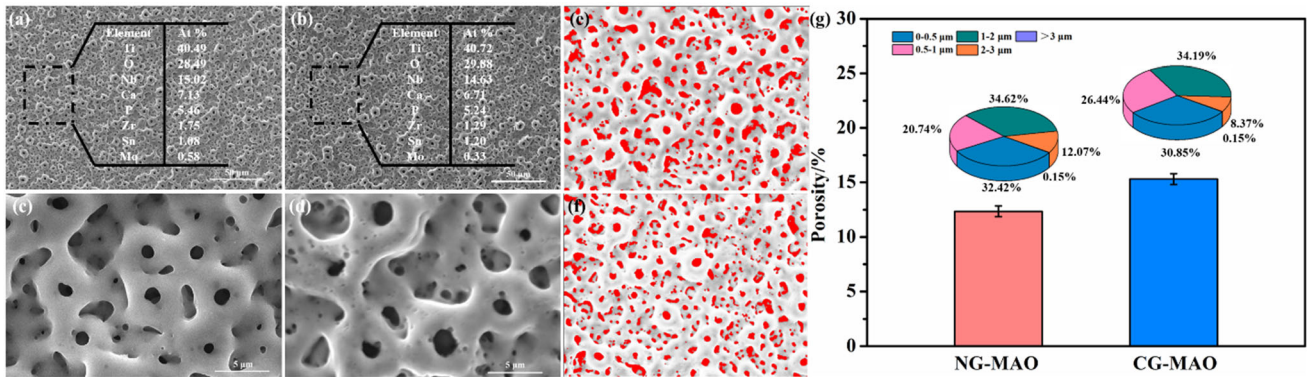


Figure 2 SEM images and EDS results of MAO coatings: **a, c** CG-MAO; **b, d** NG-MAO; SEM images treated by IPP: **e** CG-MAO, **f** NG-MAO; **g** pore size distribution and porosity statistics.

of the coatings was not significantly different. The high-magnification images in Fig. 2c and d indicated that the two MAO surfaces were full of micro-pores, but there were a large number of submicron micro-pores around the macropores of NG-MAO coating. In contrast, the surface of CG-MAO coating showed much fewer submicron pores.

Figure 2e and f shows the characteristics of micropores of the CG-MAO and NG-MAO coatings after IPP software treatment. The statistical results in Fig. 2g indicated that the average porosity of NG-MAO coating was 12.36%, which was lower than that of CG-MAO coating (15.3%). These might be due to the fact that there were more submicron pores on the surface of NG-MAO coating, but the number of pores with larger size was less.

The longitudinal-section SEM images of the CG-MAO and NG-MAO coatings in Fig. 3a and b presented that the NG-MAO coating was slightly thicker than the CG-MAO coating. The EDS results of the CG-MAO and NG-MAO coatings as shown in Fig. 3c and d revealed that there was a boundary between TLM alloy substrate and the two coatings. As can be seen from the revised EDS results in Fig. 3d, the change of Ti content at the interface between the NG-MAO coating and substrate was milder and more gradually as compared with the CG-MAO coating, indicating that there was a better “buffer transition zone” between the NG-MAO coating and substrate. These two coatings had the same phase composition, including rutile TiO₂, anatase TiO₂ and CaTiO₃, as well as a small amount of other amorphous phases (Fig. 3e). The XPS spectra in Fig. 3f displayed there was no significant difference between the two coatings, which were consistent with those of XRD and

EDS results, indicating that SFT had no significant effect on the phase composition of MAO coating.

The surface morphology and roughness of MAO coatings via AFM are shown in Fig. 4. Figure 4a and c presents the three-dimensional and two-dimensional morphology of the CG-MAO coating, and Fig. 4b and d shows the three-dimensional and two-dimensional morphology of the NG-MAO coating, respectively. The CG-MAO and NG-MAO coatings had similar morphology, but the surface roughness Ra and Rq of the NG-MAO coating was 704 and 878 nm, respectively, significantly higher than those of CG-MAO coating of 537 and 657 nm, respectively (Fig. 4e).

Electrochemical corrosion behavior

Figure 5a and c presents the OCP curves of the CG-MAO and NG-MAO coatings in PS solution and SBF solution, respectively. The potentials of the two coatings were stable in both solutions. The OCPs of the NG-MAO coating in PS solution and SBF solution were 0.284 and 0.113 V, significantly higher than those of the CG-MAO coating of 0.158 V and 0.085 V.

Figure 5b and d shows the polarization curves of the CG-MAO coating and the NG-MAO coating in PS solution and SBF solution, respectively. Table 2 shows the electrochemical corrosion test results of the two coatings in both PS and SBF solutions. The corrosion current density (I_{corr}) of NG-MAO coating was 103 nA/cm², which was significantly lower than that of CG-MAO coating (182 nA/cm²) in PS. In addition, the polarization resistance of NG-MAO coating was $1.03 \times 10^5 \Omega \text{ cm}^2$, which was much higher than that of CG-MAO ($5.1 \times 10^4 \Omega \text{ cm}^2$). The same trend was demonstrated in SBF. The I_{corr} of NG-MAO coating

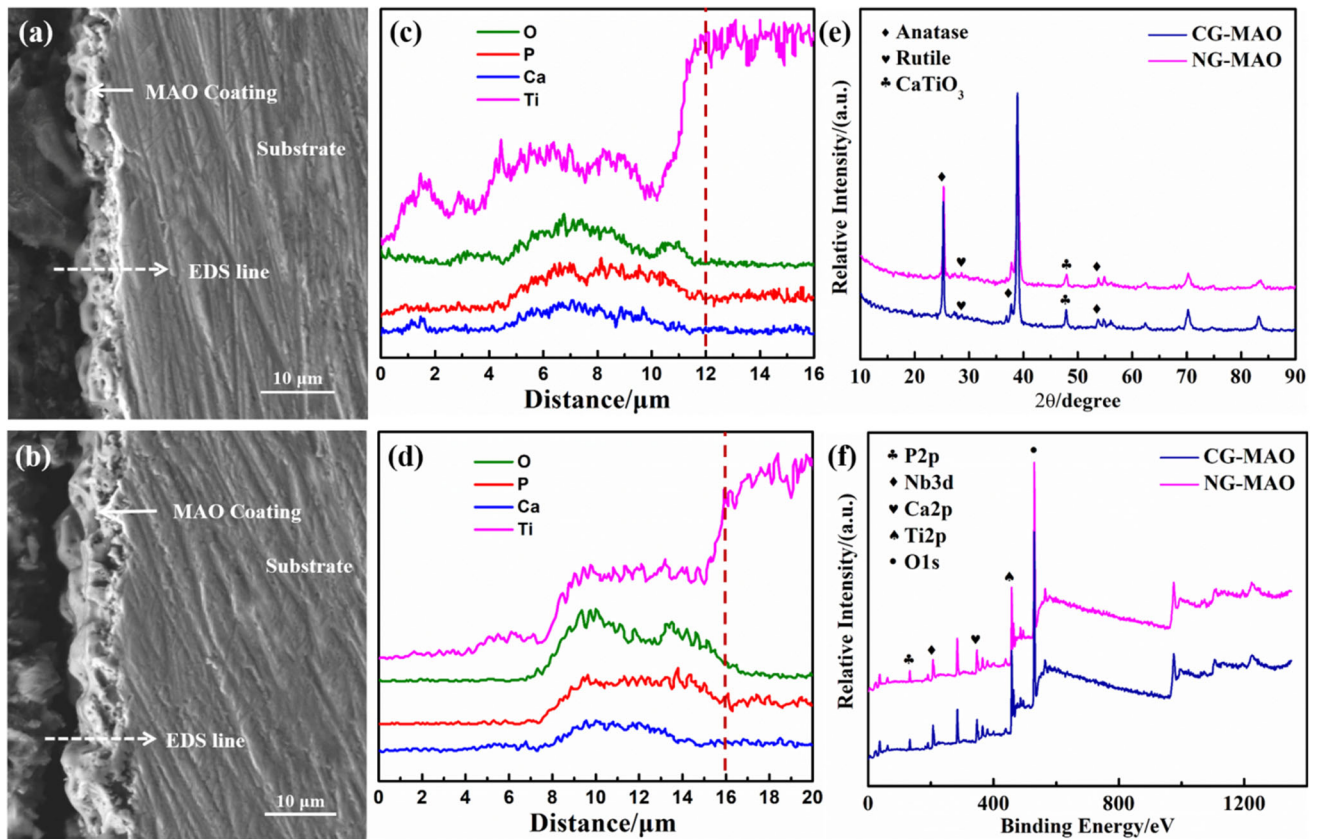


Figure 3 The cross-sectional SEM images of MAO coatings: **a** CG-MAO; **b** NG-MAO; element distribution curve of coating section: **c** CG-MAO; **d** NG-MAO; the phase composition and element characteristics of CG-MAO coating and NG-MAO coating: **e** XRD, **f** XPS.

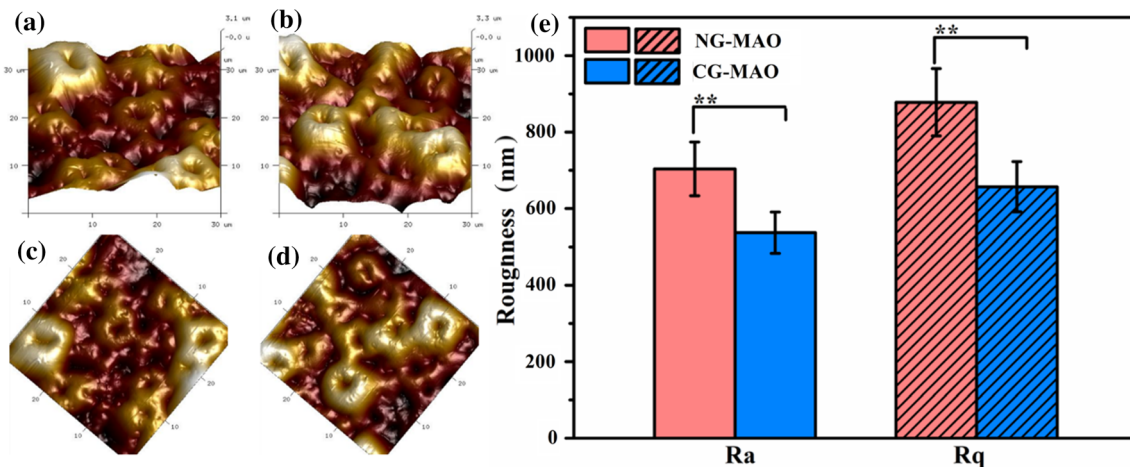


Figure 4 AFM images of the **a, c** CG-MAO and **b, d** NG-MAO coatings, and **e** surface roughness of the two coatings.

was 178 nA/cm^2 , almost half of that of CG-MAO coating (334 nA/cm^2). The polarization resistance of NG-MAO coating was $1.3 \times 10^5 \Omega \text{ cm}^2$, which was much higher than that of CG-MAO coating ($6.3 \times 10^4 \Omega \text{ cm}^2$).

Figure 6a and b presents the Nyquist and Bode diagrams of the CG-MAO coating and the NG-MAO coating in PS solution, respectively. The semicircle curve in the Nyquist diagram represented the capacitive arc. The larger capacitive arc radius is related to the better corrosion resistance. The

Figure 5 Electrochemical measurements of the CG-MAO and NG-MAO samples in a, b PS and c, d SBF solutions: a, c open-circuit potential; b, d potentiodynamic polarization curves.

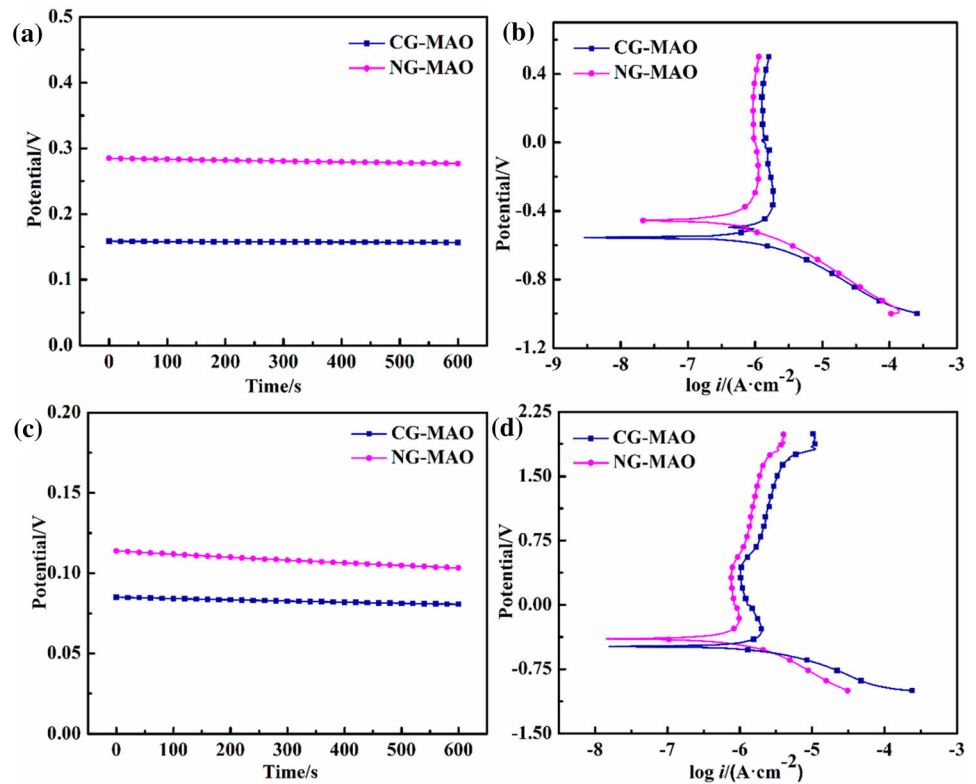


Table 2 The electrochemical corrosion parameters of CG-MAO and NG-MAO samples immersed in PS and SBF solutions

Samples	Solution	E_{corr} (V vs. SCE)	I_{corr} (nA cm ⁻²)	β_c (mV dec ⁻¹)	β_a (mV dec ⁻¹)	R (Ω cm ²)
CG-MAO	PS	-0.547	182	58.2	34	5.1×10^4
NG-MAO	PS	-0.454	103	41.4	59.6	1.03×10^5
CG-MAO	SBF	-0.458	334	90.8	104	6.3×10^4
NG-MAO	SBF	-0.394	178	93.8	117	1.3×10^5

capacitive arc radius of the NG-MAO coating was slightly larger than that of the CG-MAO coating (Fig. 6a), indicating the better corrosion resistance of NG-MAO. The curve referred to the left vertical axis in Fig. 6b showed the change of impedance mode values of the two coatings with disturbance frequency. The larger the impedance modulus value, the better the corrosion resistance. The impedance modulus value of the NG-MAO sample at low frequency was larger, suggesting that it was more corrosion resistant. The curve referred to the right vertical axis in Fig. 6b showed the change of the phase angles of the two coatings with the disturbance frequency. The larger and wider the phase angle is, the better the corrosion resistance of the material is. The phase angle of NG-MAO coating was slightly

wider and larger than that of CG-MAO at low-frequency stage. All these electrochemical testing results indicated that the NG-MAO coating had better corrosion resistance than that of the CG-MAO coating in PS solution. Likewise, Fig. 6c and Fig. 6d reveal that the corrosion resistance of the NG-MAO coating was better than that of the CG-MAO coating in SBF solution.

Figure 7 shows the equivalent analog circuit diagram of EIS of CG-MAO coating and NG-MAO coating in PS and SBF solutions. In the equivalent circuit fitting, R_s was the resistance of the corrosion solution. C_{mc} and R_{mc} represented the capacitance and corresponding resistance of the MAO coating, respectively. Q_p and R_p were the capacitance and the corresponding resistance of passivation layer,

Figure 6 EIS curves of the CG-MAO and NG-MAO samples in **a, b** PS solution and **c, d** SBF solution: **a, c** Nyquist plot; **b, d** Bode plot.

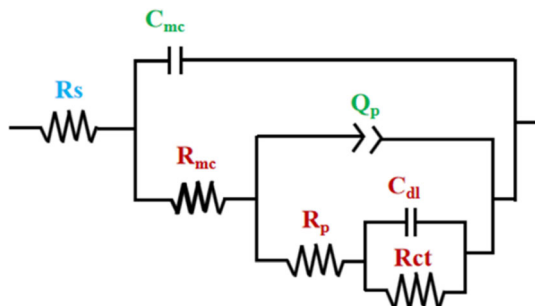
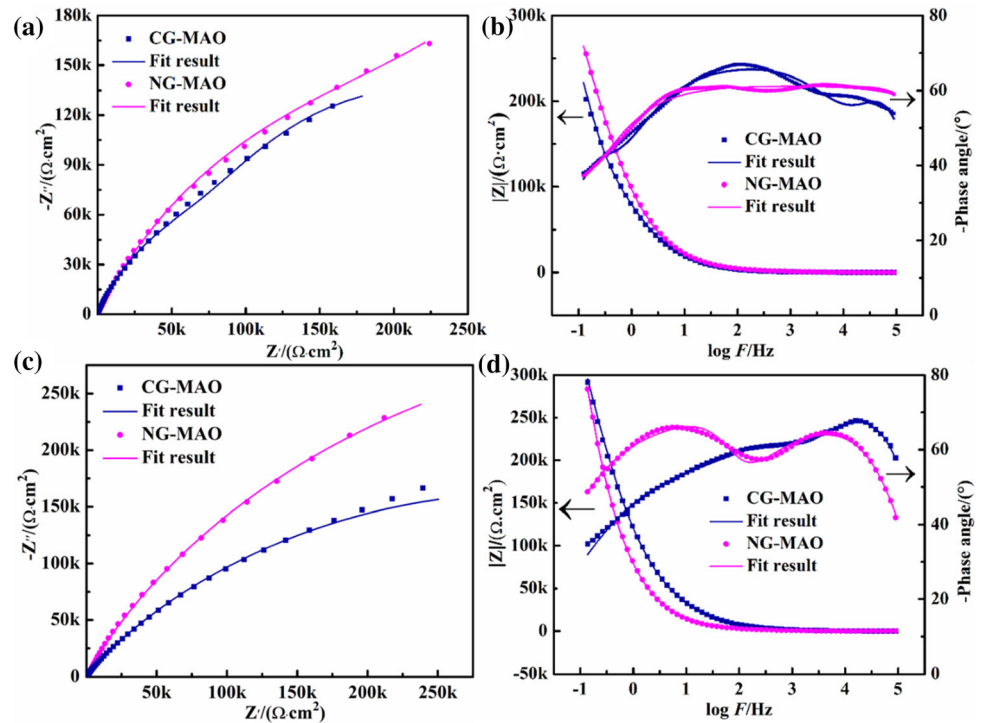


Figure 7 The equivalent circuit of the CG-MAO and NG-MAO samples in PS and SBF solutions.

respectively. C_{dl} was the capacitance corresponding to the electric double layer at the interface between the substrate and the corrosion solution, and R_{ct} represented the charge transfer resistance. The Chi-square (χ^2) value of the fitting circuit diagram selected by combining with the structure of modified layer was 10^{-4} orders of magnitude in both corrosion environments, indicating the high accuracy of the selected fitting circuit and the modified results. In the equivalent fitting circuit, the stable state of the MAO coatings could also be expressed by the polarization resistance (R_{pr}). The larger the R_{pr} value, the better the corrosion resistance of the coating [32]. Table 3 implies the fitting parameters of each circuit element of the NG-MAO and CG-MAO samples in the PS and

SBF solutions, $R_{pr} = R_{mc} + R_p + R_{ct}$. The R_{pr} of the NG-MAO coating was $9.05 \times 10^5 \Omega \text{ cm}^2$, twice more than that of the CG-MAO coating ($4.07 \times 10^5 \Omega \text{ cm}^2$) in PS. The R_{pr} of the NG-MAO coating was $9.72 \times 10^5 \Omega \text{ cm}^2$ in the SBF solution, which was also much higher than that of the CG-MAO coating ($6.49 \times 10^5 \Omega \text{ cm}^2$). Therefore, much higher R_{pr} values of the NG-MAO sample in both solutions indicated its better corrosion resistance than that of the CG-MAO coating.

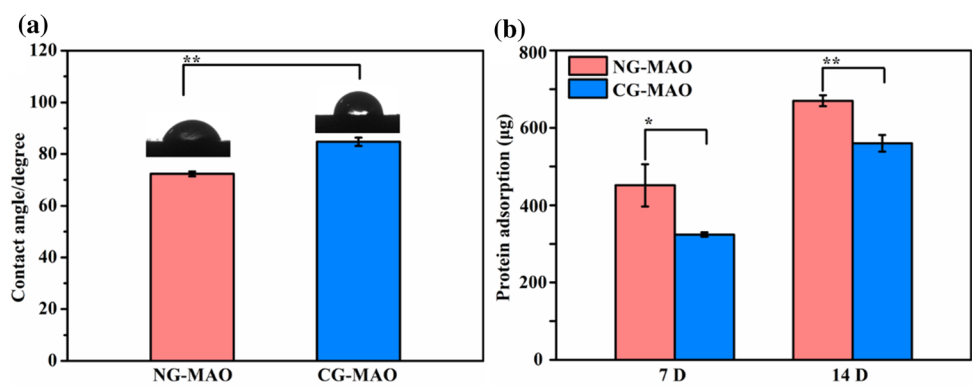
Hydrophilicity and protein adsorption of MAO coatings

Figure 8a shows the water contact angle results of the CG-MAO and NG-MAO coatings. A lower contact angle of NG-MAO coating indicated its better hydrophilicity than that of the CG-MAO coating. Figure 8b shows the statistical results of protein adsorption experiments on the two coatings. It could be found that after incubation for 7 and 14 days, the amount of protein adsorbed on the NG-MAO coating was significantly higher than that on the CG-MAO coating, demonstrating that the NG-MAO coating had better protein adsorption capacity than that of the CG-MAO coating.

Table 3 EIS fitting parameters of CG-MAO and NG-MAO samples in PS and SBF solutions

Samples	Solution	R_s/Ω cm^2	$C_{mce}/\mu\text{F}$ cm^{-2}	R_{mce}/Ω cm^2	$Q_p/\mu\text{F}$ cm^{-2}	n_b	$R_p/\text{K}\Omega$ cm^2	$C_{dl}/\mu\text{F}$ cm^{-2}	$R_{ct}/\text{K}\Omega$ cm^2	R_{pr}/Ω cm^2
CG-MAO	PS	15	0.62	118	2.44	0.7	207	4.7	200	4.07×10^5
NG-MAO	PS	8.5	3.0	163.5	2.66	0.7	472	14	433	9.05×10^5
CG-MAO	SBF	22	0.031	72	24	0.6	9.5	0.014	639	6.49×10^5
NG-MAO	SBF	16	0.043	94	30	0.7	8.9	0.023	963	9.72×10^5

Figure 8 **a** The water contact angle of the CG-MAO coating and NG-MAO coating, and **b** the amount of protein adsorption on CG-MAO and NG-MAO samples ($*p < 0.05$, $**p < 0.01$).



Biocompatibility of CG-MAO and NG-MAO

Live/dead staining images of MC3T3-E1 cells inoculated on the surface of CG-MAO coating, NG-MAO coating and blank control group for 1 h are shown in Fig. 9. Figure 9a is the tissue culture plate (TCP, without material, pure culture medium) of blank control group. The number of cells on the surface of the NG-MAO coating (Fig. 9c) was more than that of the CG-MAO coating (Fig. 9b), and there was no significant difference on the number of green living

cells between the NG-MAO coating and control group.

The morphology of osteoblasts MC3T3-E1 co-cultured on the two coatings is shown in Fig. 10. After 1-day co-culture, the cells on the NG-MAO coating grew well. Most of the cells were polygonal, and a large number of highly extended and extremely long pseudopods could be observed, and some pseudopods even extended into the pores to form connections in Fig. 10c. On the CG-MAO surface, there were a smaller number of spindle cells with multi-antennae, and the length and elongation of pseudopodia were not as good as those on NG-MAO

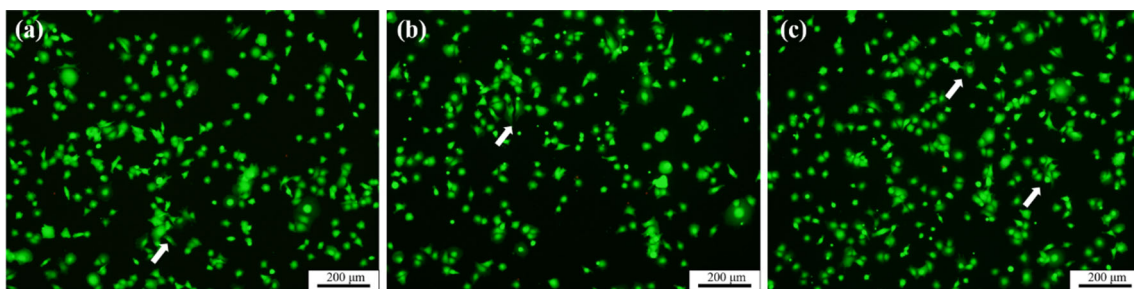
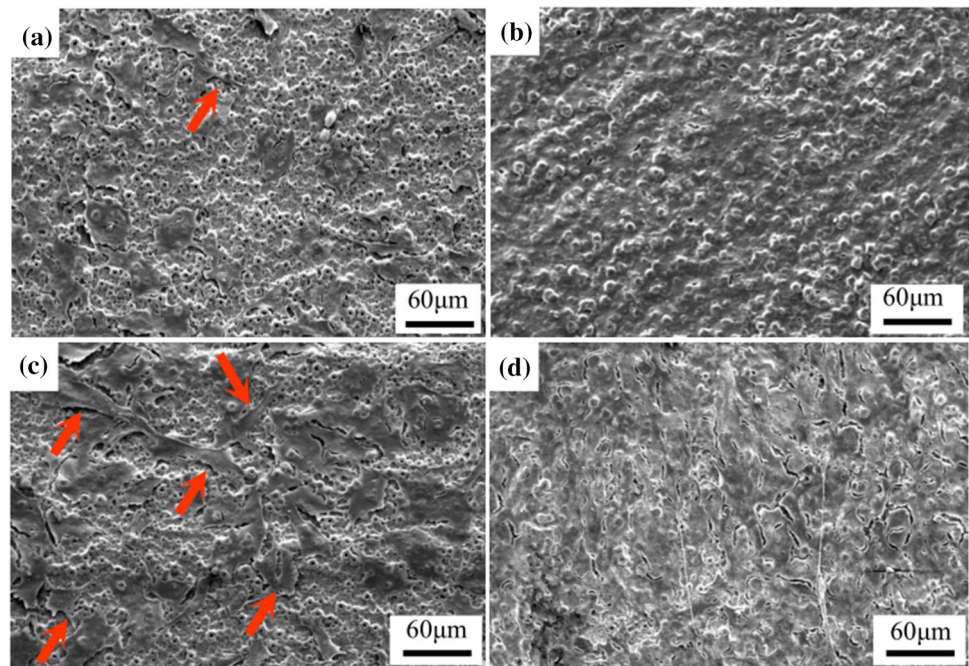


Figure 9 The cells were inoculated for 1 h with positive fluorescence microscopy: **a** TCP, **b** CG-MAO coating, and **c** NG-MAO coating.

Figure 10 SEM images of the osteoblasts cultured on **a**, **b** CG-MAO coating and **c**, **d** NG-MAO coating for **a**, **c** 1 day and **b**, **d** 3 days. Red arrows indicate filopodia extensions.



coating (Fig. 10a), indicating that the cell activity of NG-MAO coating was higher than that of CG-MAO coating. After 3 days of co-culture, osteoblasts on the two coatings spread over the whole surface, and there was no obvious difference in the number and morphology (Fig. 10b and d).

The adhesion and proliferation results of MC3T3-E1 cells co cultured on the two MAO coatings for 24 and 72 h are shown in Fig. 11. After co-culture for 24 h, all the groups displayed good adhesion and extension morphology. NG-MAO coating (Fig. 11b₁) showed a slightly larger number of cells than that of CG-MAO coating (Fig. 11a₁). After 72 h of co-culture, all the groups showed cell proliferation. The number of cells on the NG-MAO coating (Fig. 11b₂) was

significantly higher than that on the CG-MAO coating (Fig. 11a₂).

Figure 11d presents the proliferation of cells on the surface of the CG-MAO coating, the NG-MAO coating and the TCP control group quantitatively. The NG-MAO coating had good cell proliferation, slightly less than that of the TCP control group, but much higher than that of the CG-MAO coating after 1-day co-culture. After co-culture for 3 days, the cell proliferation of the TCP control group and the NG-MAO coating group presented a significant growth, while the cell proliferation rate on the CG-MAO was low. No dead cells (red fluorescence) were observed at both time points, indicating that both coatings had no obvious cytotoxicity.

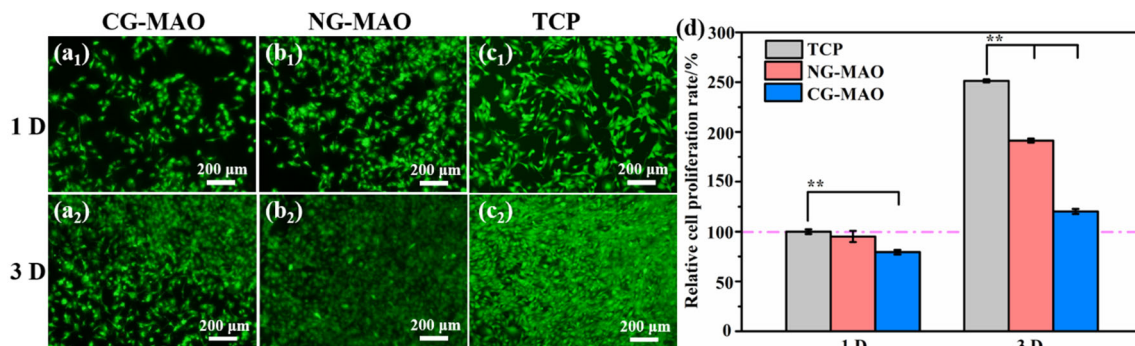


Figure 11 The normal fluorescence microscope images of osteoblasts after cultured on the samples for 1 day and 3 days: **a** CG-MAO, **b** NG-MAO, **c** TCP; **d** cell viability after incubation for 1 and 3 days.

Discussion

Most Ti alloy implants are required to serve inside the body for more than 15 years [1, 2]. The better their corrosion resistance and surface biological activity, the better their long-term biocompatibility, biological safety and osseointegration performance [7, 9]. The effectiveness of MAO to endow Ti alloys with bioactivity and improve their corrosion resistance has been proven [14, 15, 33]. In this study, the effects of surface grain refinement of the TLM alloy on microstructure, phase structure, element characteristics, corrosion resistance and biocompatibility of the MAO coating were investigated experimentally.

Before the SFT treatment, the original samples were composed of coarse $\alpha + \beta$ grains, as shown in Fig. 1. A deformed layer of a thickness of 100 μm was created on the TLM surface by SFT, as shown in Fig. 1b, and the elongated grains in the layer had an average grain size of 70 nm. This is due to the severe plastic deformation on the surface layer under the action of a mechanical load, resulting in a large number of dislocation proliferation and sliding, and the dislocations continuously cutting the matrix and enabling grain fragmentation [34]. At the same time, the increase in dislocation density leads to the increase in elastic strain energy [35]. To reduce the energy, the “broken block crystal” gradually rotates and forms nanocrystals with large-angle grain boundary [36]. The surface layer of the TLM alloy after SFT treatment was nanocrystalline, indicating that sliding friction had obvious refining effect on β -Ti alloy. The XRD diffraction peak of the SFT-treated sample displayed only a single β phase indicating the occurrence of phase transformation $\alpha \rightarrow \beta$ during SFT. Huang et al. [37] reported that: the ($\alpha + \beta$) two-phase in the TLM alloy is easier to realize surface nanocrystallization than the single β -phase TLM alloy, and with the α grain morphology changing from spherical to needle-like and increase in the content of α phase, the surface nanocrystallization of the alloy becomes easier. During the surface nanocrystallization of the ($\alpha + \beta$) alloy, strain-induced $\alpha \rightarrow \beta$ phase transformation can be induced at room temperature [34, 37]. It is believed that a large number of dislocations accumulated and gathered around the α -phase result in local stress concentration. Development of the stress gradient around the α -phase then leads to the β -phase stabilizers diffusing along the stress gradient, unestablished the α -phase

lattice and enabled α -phase dissolving into the β -matrix [31, 37].

The surface of NG-MAO exhibited much submicron pores, which might be the refined grains provided more plasma discharge channels, resulting in the formation of more micro-pores. Nanocrystals have low stability and high activity. Therefore, in the process of micro-arc oxidation, nanocrystals can reduce the discharge energy requirements and provide more reaction sites, so as to form a large number of small-size nano-micro-pores [26, 38, 39]. EDS results of the NG-MAO and CG-MAO coatings in Fig. 2 showed that both coatings contained Ca and P, indicating that all chemical ions in the electrolyte participated in the MAO process. The element contents of the NG-MAO and CG-MAO coatings in Fig. 2a and b were not significantly different, revealing that the surface nanocrystallization of TLM through SFT treatment did not significantly change the composition and content of the MAO coating, which was consistent with literature reported by Lin et al. [38].

Figure 3 demonstrates that SFT could increase the thickness of the MAO coating, as well as widen the transition zone from the oxidized coating to the substrate. This may be explained that the fine-grained structure on the surface improves the diffusion ability of elements and accelerates the electrochemical reaction on the TLM surface, contributing to a thicker MAO coating and therefore enhancing the corrosion resistance of the coating [40, 41]. In fact, the EDS curve of the NG-MAO coating was smooth at Fig. 3d, while the Ti element curve in the CG-MAO coating owned two relatively large abrupt changes (Fig. 3c). The difference of the EDS curves between the CG-MAO and NG-MAO coatings can be explained as the effect of the pores and their sizes. Figure 2 reveals that the CG-MAO coating displayed higher porosity and more micro-voids inside, and the pore size was larger, resulting in large fluctuations in the EDS curve of CG-MAO coating. The XRD and XPS results of Fig. 3e and Fig. 3f showed that both the MAO coatings contained Ca and P elements. It is well known that the coating containing Ca and P is conducive to protein adsorption and rapid adhesion and proliferation of osteoblasts, therefore enhancing the bioactivity of Ti alloy implants [40, 41]. In addition, Ca and P elements in the coating can be released into the tissue around the implant after surgery, thus increasing the calcium saturation of body fluid, so as

to accelerate the deposition of bioactive apatite on the surface of the implant, so that the implant with Ca, P coating has faster osseointegration and higher osseointegration quality [11, 12]. Severe plastic deformation on the alloy surface during the SFT induced a large number of defects to achieve grain refinement, but change could not be made to the phase composition of sequence MAO coating.

Surface morphology of Ti alloy directly affects the osseointegration rate, osseointegration quality and biological properties [11]. It can be seen from Fig. 4 that the SFT pretreatment improved the surface roughness of the coating. Previous studies have shown that nanoscale rough surface is conducive to improve the adhesion and proliferation of osteoblasts [42]. In the initial stage of osteoblast adhesion on the material surface, the developed pseudopodia with high biological activity can stretch and crawl around the nanoscale surface. The nanoscale structure provides an efficient mediating effect for cell adhesion and also accelerates cell proliferation and differentiation. Even through the mechanism of protein adsorption on nanoscale surface and enhancement of bone binding is still remained vague and imprecise, protein adhesion and cell proliferation are believed to be associated with the surface structure of the material in nanoscale [43].

Figures 5 and 6, Tables 2 and 3 show that NG-MAO coating has better corrosion resistance than the CG-MAO coating in 0.9% NaCl solution and SBF solution, indicating that grain refinement on the surface could enhance the corrosion resistance of sequenced MAO coating. It is found from Fig. 6 that CG-MAO and NG-MAO had the same phase angle at low frequency with an obvious different impedance modulus in the PS solution. Mainly because the square samples of $10 \times 10\text{mm}^2$ were used as working electrode in the electrochemical experiments with the three-electrode configuration in this study. Based on the Nyquist curve, the phase angle was controlled by different reaction steps in the low-frequency region and the high-frequency region. The low-frequency region was governed by the diffusion of reactants or products of the electrode reaction, while the high-frequency region was governed by the electrode reaction kinetics (charge transfer process). SFT refined the grain structure on the TLM alloy surface, leading to more sub-micro-pores in the NG-MAO coating. Therefore, the contact area between the electrolyte NG-MAO coating and the electrode

became larger, and a higher diffusion rate is expected in the corrosion testing than that of the CG-MAO coating. In the low-frequency region, the effect of the larger surface area of the NG-MAO coating on the diffusion rate was not significant. In contrast, the effect of the surface area on the electrode reaction kinetics is remarkable in the high-frequency region. A higher specific surface area of the NG-MAO coating results in a lower current density on the coating surface, leading to a significant difference on the phase angle between the NG-MAO and CG-MAO coatings [44–46]. The SFT treatment increased the thickness of the sequenced MAO coating because a refined surface grain structure improves the diffusion ability of elements and accelerates the electrochemical reaction rate on the TLM surface, resulting in a thicker porous oxide layer. Besides, the porosity of the NG-MAO coating is also lower than that of the CG-MAO coating. In other words, the volume of micro-pores in the coating is reduced by SFT pretreatment. Low porosity in the coating can slow down corrosive solution erosion and therefore improve corrosion resistance [35]. Some researchers also confirmed that the MAO coating formed on the surface of fine-grained Ti alloy has better corrosion resistance [25], because more structural defects in the fine-grained Ti alloy increase the nucleation position of the MAO coating, thus promoting the formation of the coating and improving uniformity and compactness of the MAO coating.

The protein adsorption capacity and cell adhesion and differentiation ability of biomaterials are directly attributed to the hydrophilicity of the material surface. Generally, the better the hydrophilic property of material, the easier cell adhesion and proliferation on the material surface [47]. The NG-MAO surface presented better hydrophilicity than the CG-MAO surface in this study. The improvement of hydrophilicity may be explained as: the refined grains of the TLM alloy after SFT provide more discharge ion channels and form more micro-pores in the MAO process so as to increase the contact area of nanocrystalline MAO coating and improve the hydrophilicity of the material surface. Meantime, protein adsorbed on the NG-MAO surface was significantly higher than that of CG-MAO coating at 7 and 14 days in Fig. 8, indicating that grain refinement improved the protein adsorption capacity of the MAO coating. Previous studies have shown that protein adsorption on substrates can regulate cell adhesion and survival [48].

Most cells are anchor-dependent cells, and they need a biocompatible matrix to attach, migrate and further differentiate, and finally form new tissues [9, 14]. Therefore, protein adsorption behavior is of great significance to evaluate the biological properties of biomaterials. The NG-MAO coating has good protein adsorption capacity, mainly because the refined grain improves coating micro-roughness and increases surface-free energy, which is conducive to the polar water molecules spreading on the coating surface, thus improving the hydrophilicity of the coating. The surface with good hydrophilicity of the NG-MAO coating is conducive to protein adsorption, and its high roughness can also promote the adsorption of protein.

Whether biomedical metal materials can produce a good biological reaction and induce the further differentiation and proliferation of new osteoblasts quickly after implantation, the premise is whether the implantable material and cells have good affinity and cell adhesion ability [11, 40]. In this study, osteoblasts (MC3T3-E1) were selected to evaluate the cell activity of the NG-MAO and CG-MAO coatings in vitro. Figure 9 shows that the adhesion ability of the NG-MAO coating was significantly higher than that of the CG-MAO coating. As shown in Fig. 2, the NG-MAO coating has higher micro-roughness and a larger number of nano- and micro-pores on the coating surface. These factors were conducive to the adhesion of osteoblasts on the surface of the coating. The cell adhesion ability is directly related to the further differentiation and proliferation of osteoblasts, so the cell proliferation ability of the NG-MAO coating is also better than that of the CG-MAO coating [49]. It is also confirmed that the response of cells to implants is not only related to the chemical composition of the material surface, but also to the micro- and nanoscale morphology of the surface [50, 51]. Although there was no obvious difference in chemical composition and phase composition between the NG-MAO and CG-MAO coatings, there were a large number of nanoscale secondary pores on the surface of the NG-MAO coating. The nanoporous structure makes the NG-MAO coating better biological activity and can accelerate cell adhesion and proliferation [52]. Simultaneously, the NG-MAO coating has better corrosion resistance, which may slow down the release of metal ions from the implant and is also conducive to the adhesion and proliferation of osteoblasts. In summary, the NG-MAO coating

significantly improves the corrosion resistance and biocompatibility of TLM alloys. By forming a micro- and nanoporous structure on the surface and introducing bioactive elements P and Ca, the surface-modified TLM alloy is expected to perform well for hard tissue repair and replacement.

Conclusion

A nanocrystalline layer with a thickness of 100 μm was produced by sliding friction treatment (SFT) on the surface of a β -titanium Ti3Zr2Sn3Mo25Nb (TLM) alloy. The micro-arc oxidation treatment (MAO) was conducted on the surfaces with and without SFT. Compared with the MAO coating on the non-SFT surface, the nanocrystalline layer did not cause obvious changes on the chemical composition of the MAO coating, but reduced the coating porosity and increased the coating thickness, leading to better corrosion resistance. With its favorable porous structure and roughness for cells to adhere and grow in, and enhanced hydrophilicity to absorb proteins, the nanocrystalline MAO coating demonstrated better cellular biocompatibility than that of the coarse-grained MAO coating. In conclusion, the combination of surface treatments of SFT and MAO was an effective way to improve both corrosion resistance and biocompatibility of TLM alloy.

Acknowledgements

The authors acknowledge the financial support of the National Natural Science Foundation of China (32071327), National Key Research and Development Program of China (2016YFC1102003), International Science and Technology Cooperation Base of Shaanxi Province (2017GHJD-014) and Science and Technology Program of Shaanxi Province (2019GY-200). And G.W. was grateful for the support from the Queensland Centre for Advanced Materials Processing and Manufacturing (AMPAM) and the ARC Research Hub for Advanced Manufacturing of Medical Devices.

Declaration

Conflict of interest The authors declare no competing financial interest.

References

- [1] Geetha M, Singh AK, Asokamani R, Gogia AK (2008) Ti based biomaterials, ultimate choice for orthopedic implants. *Prog Mater Sci* 54:397–425. <https://doi.org/10.1016/j.pmatsci.2008.06.004>
- [2] Kaur M, Singh K (2019) Review on titanium and titanium based alloys as biomaterials for orthopaedic applications. *Mater Sci Eng C* 102:844–862. <https://doi.org/10.1016/j.msec.2019.04.064>
- [3] Sidhu SS, Singh H, Gepreel MAH (2020) A review on alloy design, biological response, and strengthening of β -titanium alloys as biomaterials. *Mater Sci Eng C* 121:111661. <https://doi.org/10.1016/j.msec.2020.111661>
- [4] Fu YB, Chen HN, Guo RQ, Huang YD, Yabo Fu, Mohammad RT (2021) Extraordinary strength-ductility in gradient amorphous structured Zr-based alloy. *J Alloys Compd* 888:161507. <https://doi.org/10.1016/j.jallcom.2021.161507>
- [5] Xu XX, Jia ZJ, Zheng YF, Wang YJ (2021) Bioadaptability of biomaterials: Aiming at precision medicine. *Matter* 4:2648–2650. <https://doi.org/10.1016/j.matt.2021.06.033>
- [6] Tardelli JDC, Bolfarini C, Dos Reis AC (2020) Comparative analysis of corrosion resistance between beta titanium and Ti-6Al-4V alloys: a systematic review. *J Trace Elem Med Biol* 62:126618. <https://doi.org/10.1016/j.jtemb.2020.126618>
- [7] Ibrahim MZ, Sarhan AAD, Yusuf F, Hamdi M (2017) Biomedical materials and techniques to improve the tribological, mechanical and biomedical properties of orthopedic implants—a review article. *J Alloys Comps* 714:636–667. <https://doi.org/10.1016/j.jallcom.2017.04.231>
- [8] Pjetursson BE, Thoma D, Jung R, Zwahlen M, Zembic A (2012) A systematic review of the survival and complication rates of implant-supported fixed dental prostheses (FDPs) after a mean observation period of at least 5 years. *Clin Oral Implants Res* 23:22–38. <https://doi.org/10.1111/j.1600-0501.2012.02546.x>
- [9] Devgan S, Sidhu SS (2019) Evolution of surface modification trends in bone related biomaterials: a review. *Mater Chem Phys* 233:68–78. <https://doi.org/10.1016/j.matchemphys.2019.05.039>
- [10] Aglietta M, Iorio Siciliano V, Blasi A, Sculean A, Brägger U, Lang NP, Salvi GE (2012) Clinical and radiographic changes at implants supporting single-unit crowns (SCs) and fixed dental prostheses (FDPs) with one cantilever extension. A retrospective study. *Clin Oral Implants Res* 23:550–555. <https://doi.org/10.1111/j.1600-0501.2011.02391.x>
- [11] Wysotzki P, Sancho A, Gimsa J, Groll J (2020) A comparative analysis of detachment forces and energies in initial and mature cell-material interaction. *Colloids Surf B* 190:110894. <https://doi.org/10.1016/j.colsurfb.2020.110894>
- [12] Yu S, Yu ZT, Wang G, Han JY, Ma X, Dargusch MS (2011) Biocompatibility and osteoconduction of active porous calcium-phosphate films on a novel Ti-3Zr-2Sn-3Mo-25Nb biomedical alloy. *Colloids Surf B* 85:83–115. <https://doi.org/10.1016/j.colsurfb.2011.02.025>
- [13] Deng CH, Shen XK, Yang WH, Luo Z, Ma PP, Shen TT, Liu J, Cai KY (2018) Construction of zinc-incorporated nano-network structures on a biomedical titanium surface to enhance bioactivity. *Appl Surf Sci* 453:263–270. <https://doi.org/10.1016/j.apsusc.2018.05.097>
- [14] Kurup A, Dhatrik P, Khasnis N (2021) Surface modification techniques of titanium and titanium alloys for biomedical dental applications: a review. *Mater Today Proc* 39:84–90. <https://doi.org/10.1016/j.matpr.2020.06.163>
- [15] Zhang LC, Chen LY, Wang LQ (2020) Surface modification of titanium and titanium alloys: technologies, developments, and future interests. *Adv Eng Mater* 22:2070017. <https://doi.org/10.1002/adem.201901258>
- [16] Wang YJ (2016) Bioadaptability: an innovative concept for biomaterials. *J Mater Sci Technol* 32:801–809. <https://doi.org/10.1016/j.jmst.2016.08.002>
- [17] Yu S, Yu Z, Guo DG, Zhu H, Zhang MH, Han JY, Zhe Yu, Yu ZT et al (2022) Enhanced bioactivity and interfacial bonding strength of Ti3Zr2Sn3Mo25Nb alloy through graded porosity and surface bioactivation. *J Mater Sci Technol* 100:137–149. <https://doi.org/10.1016/j.jmst.2021.06.008>
- [18] Wang L, Zhou WH, Yu ZT, Yu S, Zhou L, Cao YM, Dargusch M, Wang G (2021) An in vitro evaluation of the hierarchical micro/nanoporous structure of a Ti3Zr2Sn3Mo25Nb Alloy after surface dealloying. *ACS Appl Mater Interfaces* 13:15017–15030. <https://doi.org/10.1021/acsami.1c02140>
- [19] Liu XY, Chu PK, Ding CX (2004) Surface modification of titanium, titanium alloys, and related materials for biomedical applications. *Mater Sci Eng R Rep* 47:49–121. <https://doi.org/10.1016/j.mser.2004.11.001>
- [20] Song C, Liu M, Deng ZQ, Niu SP, Deng CM, Liao HL (2018) A novel method for in-situ synthesized TiN coatings by plasma spray-physical vapor deposition. *Mater Lett* 217:127–130. <https://doi.org/10.1016/j.matlet.2018.01.068>
- [21] Yu S, Guo DG, Han JY, Sun LJ, Zhu H, Yu ZT, Dargusch M, Wang G (2020) Enhancing antibacterial performance and bioactivity of pure titanium by a two-step electrochemical surface coating. *ACS Appl Mater Interfaces* 12:44433–44446. <https://doi.org/10.1021/acsami.0c10032>
- [22] Doe Y, Ida H, Seiryu M et al (2020) Titanium surface treatment by calcium modification with acid-etching promotes osteogenic activity and stability of dental implants.

- Materialia 12:100801. <https://doi.org/10.1016/j.mtla.2020.100801>
- [23] Cao Y, Dhahad HA, El-Shorbagy MA, Alijani HQ, Zakeri M, Heydari A, Bahonar E, Slouf M et al (2021) Green synthesis of bimetallic ZnO–CuO nanoparticles and their cytotoxicity properties. *Sci Rep* 11:23479. <https://doi.org/10.1038/s41598-021-02937-1>
- [24] Hu MR, Wang YF, Yan ZF, Zhao YX, Xia L, Bowen C, Di YB, Zhuang XP (2021) Hierarchical dual-nanonet of polymer nanofibers and supramolecular nanofibrils for air filtration with high filtration efficiency, low air resistance and high moisture permeation. *J Mater* 24. <https://doi.org/10.1039/D1TA01505B>
- [25] Gu YH, Chen LL, Yue W, Chen P, Chen F, Ning CY (2016) Corrosion behavior and mechanism of MAO coated Ti6Al4V with a grain-fined surface layer. *J Alloys Compd* 664:770–776. <https://doi.org/10.1016/j.jallcom.2015.12.108>
- [26] Huo WT, Lin X, Cao HH, Yu S, Yu ZT, Zhang YS (2018) Manipulating the degradation behavior and biocompatibility of Mg alloy through a two-step treatment combining sliding friction treatment and micro-arc oxidation. *J Mater Chem B* 6:6431–6443. <https://doi.org/10.1039/C8TB01072B>
- [27] Uvarov V, Popov I (2007) Metrological characterization of X-ray diffraction methods for determination of crystallite size in nano-scale materials. *Mater Charact* 58:883–891. <https://doi.org/10.1016/j.matchar.2006.09.002>
- [28] Li XY, Lu L, Li JG, Zhang X, Gao HJ (2020) Mechanical properties and deformation mechanisms of gradient nanostructured metals and alloys. *Nat Rev Mater* 5:706–723. <https://doi.org/10.1038/s41578-020-0212-2>
- [29] Zhang YS, Zhang LC, Niu HZ, Bai XF, Yu S, Ma XQ, Yu ZT (2014) Deformation twinning and localized amorphization in nanocrystalline tantalum induced by sliding friction. *Mater Lett* 127:4–7. <https://doi.org/10.1016/j.matlet.2014.04.079>
- [30] Liu CQ, Chen XH, Zhang W, Zhang YS, Pan FS (2020) Microstructural evolution in the ultrafine-grained surface layer of Mg–Zn–Y–Ce–Zr alloy processed by sliding friction treatment. *Mater Charact* 166:110423. <https://doi.org/10.1016/j.matchar.2020.110423>
- [31] Yu ZT, Yu S, Ma XQ, Cheng J (2017) Development and application of novel biomedical titanium alloy materials. *Acta Metall Sin-Engl* 53: 1238–64. <https://doi.org/10.11900/0412.1961.2017.00288>
- [32] Li RY, Wei YJ, Gu L, Qin YG, Li DD (2020) Sol–gel-assisted micro-arc oxidation synthesis and characterization of a hierarchically rough structured Ta–Sr coating for biomaterials. *RSC Adv* 10:20020–20027. <https://doi.org/10.1039/D0RA01079K>
- [33] Pesode P, Barve S (2021) Surface modification of titanium and titanium alloy by plasma electrolytic oxidation process for biomedical applications: a review. *Mater Today Proc* 46:594–602. <https://doi.org/10.1016/j.matpr.2020.11.294>
- [34] Huang R, Han Y (2013) The effect of SMAT-induced grain refinement and dislocations on the corrosion behavior of Ti–25Nb–3Mo–3Zr–2Sn alloy. *Mater Sci Eng C* 33:2353–2359. <https://doi.org/10.1016/j.msec.2013.01.068>
- [35] Gheyhani M, Bagheri HR, Masiha HR, Aliofkhaezrai M (2014) Effect of SMAT preprocessing on MAO fabricated nanocomposite coating. *Surf Eng* 30:244–255. <https://doi.org/10.1179/1743294414Y.0000000251>
- [36] Jin L, Cui WF, Song X, Liu G, Zhou L (2014) Surface nanocrystalline characteristics and corrosion resistance of β -type titanium alloy. *Rare Metal Mat Eng* 43:80–84
- [37] Huang R, Zhuang HY, Han Y (2013) Second-phase-dependent grain refinement in Ti–25Nb–3Mo–3Zr–2Sn alloy and its enhanced osteoblast response. *Mater Sci Eng C* 35:144–152. <https://doi.org/10.1016/j.msec.2013.10.037>
- [38] Xu L, Wu C, Lei XC, Zhang K, Liu CC, Ding JN, Shi XL (2018) Effect of oxidation time on cytocompatibility of ultrafine-grained pure Ti in micro-arc oxidation treatment. *Surf Coat Technol* 342:12–22. <https://doi.org/10.1016/j.surfcoat.2018.02.044>
- [39] Cao HH, Huo WT, Ma SF, Zhang YS, Zhou L (2018) Microstructure and corrosion behavior of composite, coating on pure Mg acquired by sliding friction, treatment and micro-arc oxidation. *Materials* 11:1232. <https://doi.org/10.3390/ma11071232>
- [40] Li GL, Cao HL, Zhang WJ, Ding X, Yang GZ, Qiao YQ, Liu XY, Jiang XQ (2016) Enhanced osseointegration of hierarchical micro/nanotopographic titanium fabricated by micro-arc oxidation and electrochemical treatment. *ACS Appl Mater Interfaces* 8:3840–3852. <https://doi.org/10.1021/acsami.5b10633>
- [41] Zhao QM, Yi L, Jiang LB, Ma YQ, Lin H, Dong J (2019) Surface functionalization of titanium with zinc/strontium-doped titanium dioxide microporous coating via microarc oxidation. *Nanomedicine* 16:149–161. <https://doi.org/10.1016/j.nano.2018.12.006>
- [42] Souza JCM, Sordi MB, Kanazawa M, Ravindran S, Henriques B, Silva FS, Aparicio C, Cooper LF (2019) Nano-scale modification of titanium implant surfaces to enhance osseointegration. *Acta Biomater* 94:112–131. <https://doi.org/10.1016/j.actbio.2019.05.045>
- [43] Biggerelle M, Anselme K, Noël B, Ruderman I, Hardouin P, Lost A (2002) Improvement in the morphology of Ti-based surfaces: a new process to increase in vitro human osteoblast response. *Biomaterials* 23:1563–1577. [https://doi.org/10.1016/S0142-9612\(01\)00271-X](https://doi.org/10.1016/S0142-9612(01)00271-X)

- [44] Guo Y, Duan TG, Chen Y, Wen Q (2015) Solvothermal fabrication of three-dimensionally sphere-stacking Sb–SnO₂ electrode based on TiO₂ nanotube arrays. *Ceram* 41:8723–8729. <https://doi.org/10.1016/j.ceramint.2015.03.092>
- [45] Zhu WQ, Shao SY, Xu LN, Chen WQ, Yu XY, Tang KM, Tang ZH, Zhang FM et al (2019) Enhanced corrosion resistance of zinc-containing nanowires-modified titanium surface under exposure to oxidizing microenvironment. *J Nanobiotechnol* 17:55. <https://doi.org/10.1186/s12951-019-0488-9>
- [46] Balusamy T, James M, Kumar S, Sankara Narayanan TSN (2012) Corrosion resistant Ti alloy for sulphuric acid medium: suitability of Ti–Mo alloys. *Werkst Korros* 63:9. <https://doi.org/10.1002/maco.201106275>
- [47] Gheyhani M, Aliofkhaezai M, Bagheri HR, Masiha HR, Rouhaghdam AS (2015) Wettability and corrosion of alumina embedded nanocomposite MAO coating on nanocrystalline AZ31B magnesium alloy. *J Alloys Compd* 649:666–673. <https://doi.org/10.1016/j.jallcom.2015.07.139>
- [48] Wei GB, Ma PX (2004) Structure and properties of nano-hydroxyapatite/polymer composite scaffolds for bone tissue engineering. *Biomaterials* 25:4749–4757. <https://doi.org/10.1016/j.biomaterials.2003.12.005>
- [49] Mendonça G, Mendonça DBS, Aragão FJL, Cooper LF (2008) Advancing dental implant surface technology: From micro- to nanotopography. *Biomaterials* 29:3822–3835. <https://doi.org/10.1016/j.biomaterials.2008.05.012>
- [50] Richert L, Vetrone F, Yi J-H, Zalzal SF, Wuest JD, Rosei F, Nanci A (2008) Surface Nanopatterning to Control Cell Growth. *Adv Mater* 20:1488–1492. <https://doi.org/10.1002/adma.200701428>
- [51] Variola F, Vetrone F, Richert L et al (2009) Improving biocompatibility of implantable metals by nanoscale modification of surfaces: an overview of strategies, fabrication methods, and challenges. *Small* 5:996–1006. <https://doi.org/10.1002/sml.200801186>
- [52] Andrukhov O, Huber R, Shi B, Berner S, Fan XHR, Moritz A, Spencer ND, Schedle A (2016) Proliferation, behavior, and differentiation of osteoblasts on surfaces of different microroughness. *Dent Mater* 32:1374–1384. <https://doi.org/10.1016/j.dental.2016.08.217>

Publisher's Note Springer Nature remains neutral with regard to jurisdictional claims in published maps and institutional affiliations.